Quang Duy Nguyen, Hoon Cheol Park*, Taesam Kang and Jin Hwan Ko

Structural design and analysis of composite blade for horizontal-axis tidal turbine

https://doi.org/10.1515/secm-2017-0093
Received March 21, 2017; accepted October 1, 2017; previously published online November 22, 2017

Abstract: In this work, we report on the structural design of a 5-m-long composite blade intended for use in a horizontal-axis tidal turbine. The blade geometry is constructed through an optimization process to obtain the maximum power coefficient at the desired tip speed ratio of 4.5 by applying the blade element-momentum theory (BEMT). The blade is primarily designed using a NACA 63-424 hydrofoil. The blade structure is designed by using the BEMT to compute the loading conditions at various inflow velocities. Two parallel spars were chosen to produce the blade structure grid, and the preliminary lay-up structure of the composite blade was determined according to the thickness distribution identified using the twisted beam theory under the assumption that the two spars plus the upper and lower skins mostly contribute to the flap-wise bending stiffness while withstanding an external load. Then, high-strength unidirectional and double-bias fiber glass/epoxy materials were chosen to fabricate the blade. The final blade structure was then analyzed in ANSYS Workbench using the finite element method. The results show that the blade structure can withstand the applied load with failure indices <0.4.

Keywords: beam theory; composite blade; lay-up structure; loading condition; spars; structural design.

1 Introduction

Nowadays, humans face numerous environmental issues, and in the near future, fossil fuel energy and natural gas may disappear. As a result, people are searching for and developing various types of environmentally friendly replaceable and reusable energy sources, like solar energy, wind energy, tidal energy, etc. Tidal energy is a virtually infinite renewable energy source that is now being exploited in many industrialized nations. Furthermore, the generation of electrical energy using tides can be regular and predictable [1], so there has been an increase in the numbers of researches developing tidal current turbines by applying new technologies [2–9].

Many types of tidal turbines were discussed in a recent survey [10], and among those, horizontal-axis tidal turbines (HATTs) are the most widely used in real applications [11]. A similar trend can be seen in the case of wind turbines; that is, horizontal-axis wind turbines (HAWTs) are more popular [12]. In fact, designing blades for the HATT and HAWT is not much different in terms of the blade design process. The combined blade element and momentum theory (BEMT) was first used for the design of wind turbines, and then it was adopted for designing tidal turbine blades. However, as HATT is designed to operate undersea, the HATT blades can be exposed to harsh conditions, such as corrosion by salt water, fouling by marine organisms, cavitation, and probably flooding. The HATT blades are also expected to suffer from larger hydrodynamic forces than HAWT blades, as the density of seawater is about 830 times larger than that of air [13]. Therefore, HATT blades are normally fabricated using high-strength composite materials [3, 5, 6]. In fact, HATT blades are assumed to be subjected to twice the maximum velocity in a local area [3]. For these reasons, it is assumed that extreme operating conditions will occur when designing a HATT blade structure.

The blade structure must be carefully designed to endure the loads experienced in extreme environments, as the exterior and interior structures of a HATT/HAWT blade play a critical role in the whole turbine properly resisting loading and effectively producing power at the same time. In most cases, the structure is often designed with two straight parallel spars along the blade span [3, 5, 14–16] or a bending-twist couple beam is used [17]. On the other hand, the blade structure can be designed in a unique way by using biplane spars where two spars merge at the mid spar [18]. A thicker hydrofoil can be used to obtain a blade structure with a higher stiffness because a thicker hydrofoil provides a larger flap-wise bending stiffness

***Corresponding author: Hoon Cheol Park,** Department of Advanced Technology Fusion, Konkuk University, National Research Laboratory for Biomimetics and Intelligent Microsystem, 143-701 Seoul, South Korea, e-mail: hcpark@konkuk.ac.kr
Quang Duy Nguyen: Department of Advanced Technology Fusion, Konkuk University, National Research Laboratory for Biomimetics and Intelligent Microsystem, 143-701 Seoul, South Korea
Taesam Kang: Department of Aerospace Information Engineering, Konkuk University, 143-701 Seoul, South Korea
Jin Hwan Ko: Major of Mechanical Engineering, Jeju National University, 102 Jejudaehak-ro, Jeju-si, Jeju Special Self-Government Province, 63243, South Korea

than a thinner hydrofoil due to the larger second moment of inertia in the flap-wise direction for an identical blade skin thickness [5]. The root area of a blade particularly suffers from the largest flap-wise and lag-wise bending stresses, and this area is often modified to a circular cross section to mount the blade to the hub structure [14, 16, 19, 20]. Thus, higher stiffness and strength are required near the blade root area.

This paper reports a case study of the structural design of a 5-m-long HATT blade with a relatively thick NACA 63-424 hydrofoil. High-strength glass/epoxy materials were chosen to fabricate the blade instead of carbon/epoxy materials in order to prevent possible corrosion [21], which happens when the blade is assembled into a metal hub structure. Finally, the loading condition was computed by applying the BEMT code (Bimilab, Konkuk University, Seoul, South Korea) with a finite element model of the blade in ANSYS Workbench (ANSYS, Inc., Canonsburg, PA, USA) to examine the possible structural failure of the composite blade.

2 Blade geometry

Basically, the major design parameters of the turbine in this work include the turbine radius, hub radius, number of blades, inflow velocity, and desired *TSR*, as shown in Table 1.

The blade geometry was designed using the BEMT program to have a maximum power coefficient at a *TSR* of 4.5 [22]. The BEMT code exports the chord length and twist angle distribution that defines the blade geometry using a NACA 63-424 hydrofoil. Figure 1 shows the chord length and twist angle distributions that were finally determined. The blade geometry in Figure 1 shows a modified version of the originally optimized geometry, such that the blade twist angle is constant from the root to 25%*R*. Furthermore, a chord length of up to 25%*R* was reduced to remove excessively long trailing edges. The three-dimensional computer-aided design (CAD) image of the final blade geometry is shown in Figure 2.

Table 1: Turbine information.

Parameters	Symbols	Details
Radius of turbine	R	6 m
Radius of hub	r_h	1 m
Number of blades	B	3
Inflow velocity	V	2.3 m/s
Tip speed ratio	*TSR*	4.5
Hydrofoil	–	NACA 63-424

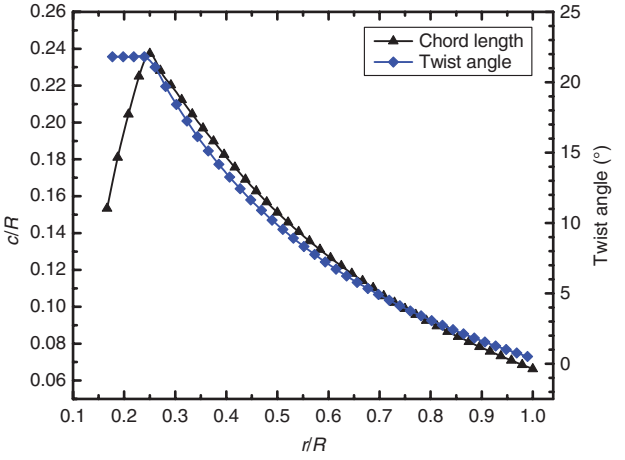

Figure 1: Chord length and twist angle distribution of the blade.

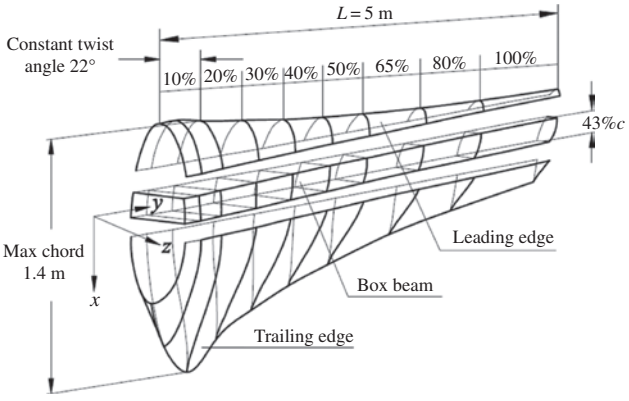

Figure 2: CAD image of the final blade geometry.

The spar structure includes front and rear spars that are parallel to each other, and the distance between the two spars is 43% of the tip chord. Inside the blade, the two-spar structure and blade skin can be simply modeled as a box beam with a rectangular cross section, and the box beam in the blade is assumed to provide most of the flap-wise bending stiffness, so the preliminary thickness distribution can be first chosen using the beam theory [23].

3 Loading condition

The primary loads acting on the blade are the hydrodynamic lift, drag, and pitching moment. The lift and drag are decomposed into the element thrust force (dF_z) and element tangential force (dF_x), as shown in Figure 3.

Here, a, a', α, β, and φ are the axial induction factor, angular induction factor, effective angle of attack, blade twist angle, and inflow angle, respectively. The lift (dL)

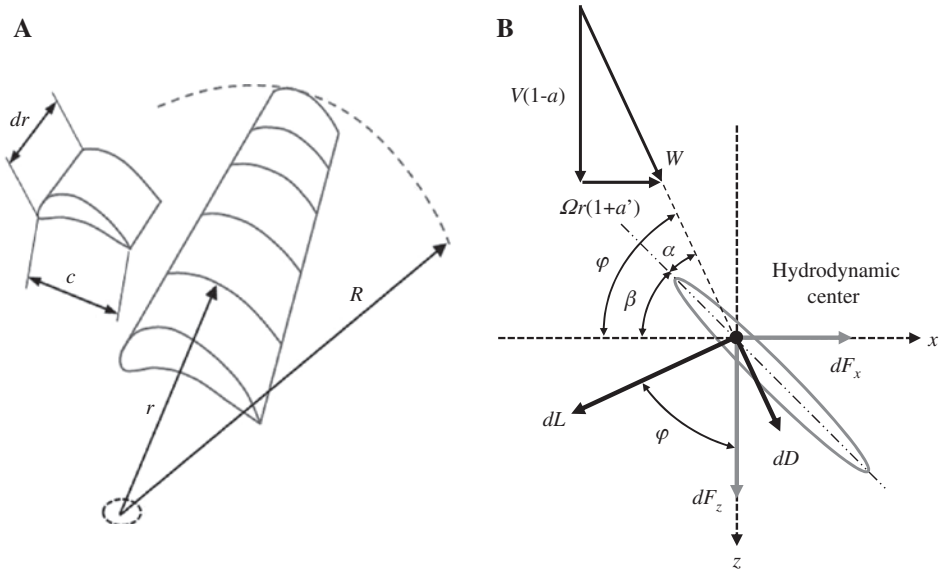

Figure 3: Hydrodynamic forces acting on a blade element [22]. (A) Blade element. (B) Flow into the turbine blade and forces.

and drag (*dD)* acting on the blade element are determined using the following equations [24]:

$$dL = \frac{1}{2}\rho C_L W^2 c dr, \tag{1}$$

$$dD = \frac{1}{2}\rho C_D W^2 c dr, \tag{2}$$

where C_L, C_D, c, dr, ρ, and W are the lift and drag coefficients, chord length, width of the blade element, water density, and resulting velocity, respectively.

The element lift and drag contribute to the element thrust (dF_z) and element tangential force (dF_x), as follows:

$$\begin{aligned} dF_z &= B(dL\cos\varphi + dD\sin\varphi) \\ &= \frac{1}{2}\rho cBW^2(C_L\cos\varphi + C_D\sin\varphi)dr, \end{aligned} \tag{3}$$

$$\begin{aligned} dF_x &= B(dD\cos\varphi - dL\sin\varphi) \\ &= \frac{1}{2}\rho cBW^2(C_D\cos\varphi - C_L\sin\varphi)dr, \end{aligned} \tag{4}$$

where B and r are the number of blades and radial location, respectively.

The pitching moment acting on a blade element can be expressed as follows [25]:

$$dM = \frac{1}{2}\rho C_M W^2 c^2 dr. \tag{5}$$

The element thrust (dF_z) is the force acting on a blade element in the z direction, and the element tangential force (dF_x) is the force in the x direction. The element pitching moment creates torque around the y axis. As the inflow velocity is definitely not constant in real-world use, it is necessary to use the BEMT program to study loading conditions with velocities larger than the regular velocity of 2.3 m/s, including 2.5, 3.0, 3.5, 4.0 and 4.5 m/s. However, in the case of a velocity of >2.3 m/s, the blades must be pitched to another angle to reduce the thrust force and avoid cavitation [3]. According to change in the velocity of the tide, the blade is supposed to adjust the blade pitch angle to maintain a constant rotational speed of the turbine or keep the power generation steady. Depending on the pitch angle for various inflow velocities, hydrodynamic forces acting on a blade are also modified. Therefore, we need to compute the

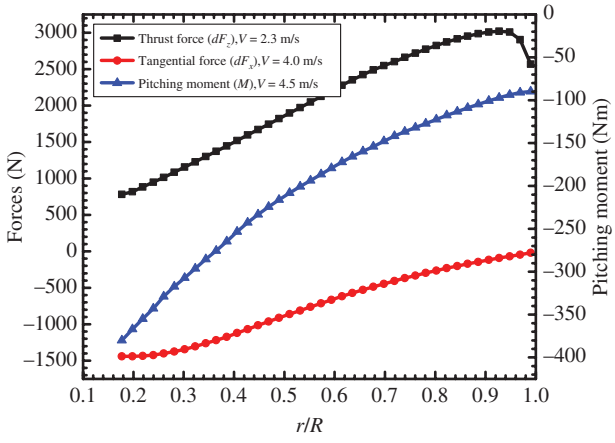

Figure 4: Loading conditions for the turbine blade.

forces for all cases of inflow velocities under corresponding pitch controls and find out the maximum loading condition among the computed load cases. Through this process, we could identify that the thrust force for $V = 2.3$ m/s, tangential force for $V = 4.0$ m/s and pitching moment for $V = 4.5$ m/s were extreme loading conditions. The loading conditions are shown in Figure 4.

Compared to wind turbine blades, tidal turbine blades are thick and short. Even though we did not exactly examine the effect of warping on structural integrity, we decided not to consider warping due to the structural characteristics of our tidal blade. In addition, as the blade axis is placed at the hydrodynamic center, the effect of torsion could be minimized.

4 Beam theory

To determine the preliminary blade thickness distribution using the beam theory, we first assume that the blade structure is made of an isotropic material and model it as a twisted cantilever beam fixed at the blade root. The blade is simplified as a non-uniform box beam made of two spars and upper and lower skins with a variable cross-sectional area from root to tip. Figure 5 shows an isometric view of the twisted cantilever beam made of two spars and skins. The distance between the two spars is 43% of the tip chord, and the beam length (L) is 5 m, with a height of the hydrofoil for each element.

Although the element thrust force is assumed to act at the hydrodynamic center of the blade, the hydrodynamic center does not coincide with the center of the rectangular cross section of the beam. To apply the beam theory, the element thrust force (dF_z) is applied at the center of each element in the $x'z'$ coordinate system in Figure 5, and the resulting pitching moment of each

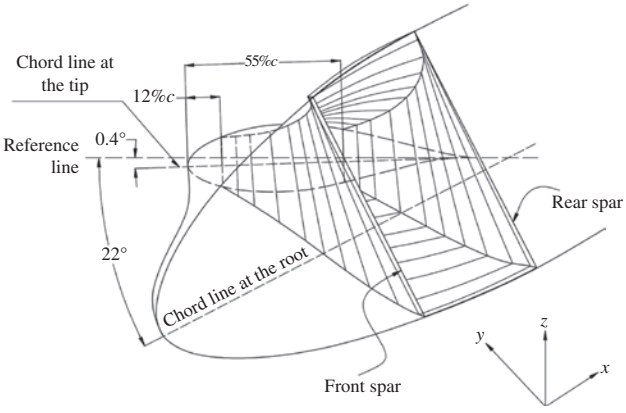

Figure 5: Isometric view of the twisted cantilever beam.

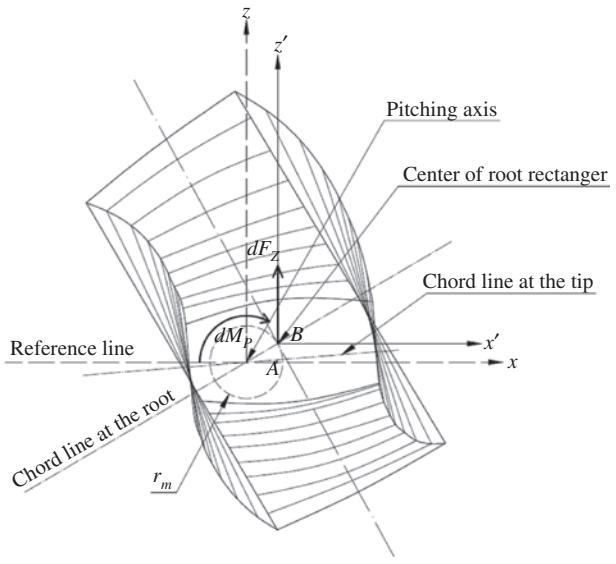

Figure 6: Front view of the twisted box beam model.

blade element (dM_p) is computed at the hydrodynamic center of each blade section. The centers for the rectangular cross sections move in a circle with a radius of $r_m = 33.3$ mm, as shown in Figure 6. Therefore, the resulting element pitching moment (dM_p) can be expressed as follows:

$$dM_P = dF_z r_m, \tag{6}$$

$$M_p = \sum_{i=1}^{N} (dF_z)_i (r_m)_i, \tag{7}$$

where N is the number of blade elements. Thus, the pitching moment computed via BEMT decreases due to the moments resulting from the beam model.

The element thrust force along the blade span creates a flap-wise bending moment and stress inside the blade structure. In contrast, the element tangential force makes the blade rotate with an angular velocity (Ω), and the pitching moment produces torsion. The element tangential force also contributes to the lag-wise bending moment and bending stress. However, the magnitude of the element tangential force is smaller than that of the element thrust. For example, dF_z is 3–10 times larger than dF_x between 57.3% and 80.2%R. In addition, the lag-wise second moment of inertia is much larger than the flap-wise second moment of inertia. Therefore, the contribution of dF_x to the bending stress is ignored to simplify the stress computation. Consequently, only the computation element thrust force (dF_z) is applied to investigate the bending stress of the structure.

Figure 7 shows the beam model for the blade and its free body diagram. By applying the beam theory, the

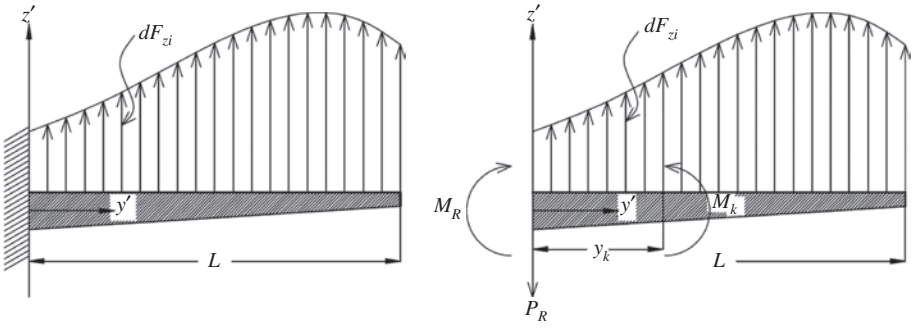

Figure 7: Modeled cantilever beam acting by the element thrust force.

reaction force and reaction moment at a fixed end can be determined as follows:

$$P_R = \sum_{i=1}^{N} dF_{zi}, \tag{8}$$

$$M_R = \sum_{i=1}^{N} dF_{zi} y_i, \tag{9}$$

where P_R and M_R are the reaction force and reaction moment at the fixed end, respectively, and dF_{zi}, y_i are the element thrust force and radial location at each blade element. The reaction force and moment were used to examine the flap-wise moment M_k, as follows:

$$M_k = M_R - P_R y_k + \sum_{i=1}^{k-1} dF_{zi} y_i, \tag{10}$$

where M_k, y_k are the bending moment and radial location of the kth element, respectively.

In the next step, we consider the moment of inertia of the twisted beam with a thickness t at locations of 0%, 20%, 40%, 60%, 80% and 100% for the beam. Basically, the moment of inertia for a hollow rectangular shape can be calculated as in Figure 8 using the 1–2 coordinate system, as follows:

$$I_1 = \frac{BH^3 - bh^3}{12}, \tag{11}$$

$$I_2 = \frac{HB^3 - hb^3}{12}, \tag{12}$$

$$I_{12} = 0, \tag{13}$$

where I_1, I_2 are the moments of inertia with respect to the 1 and 2 axes, respectively, and I_{12} is the product of inertia. The symbols B, b, H, h, and θ are the lengths of the edges for the hollow rectangular and rotational angle, respectively. The symbol β in Figure 8 stands for the twist angle.

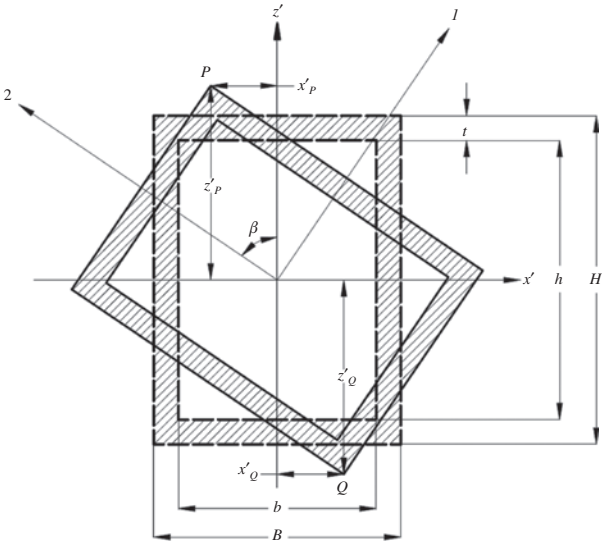

Figure 8: Coordinate system of the twisted beam (x'_P, z'_P, x'_Q, z'_Q are the coordinates for points P and Q, respectively, and t is the thickness of the hollow rectangular shape).

We assumed that the box beam structure is mostly made of unidirectional (UD) glass fiber materials without a core. In this case, the elastic constant of the beam is close to the elastic modulus in the fiber direction. Thus, we regard the beam to be made of an isotropic material with an elastic constant for the UD.

The moment of inertia in the $x'z'$ coordinate system can be computed using Eqs. (14), (15), and (16) [26]:

$$I_{zz} = \frac{I_1 + I_2}{2} - \frac{I_1 - I_2}{2} \cos(2\theta) + I_{12} \sin(2\theta), \tag{14}$$

$$I_{xx} = \frac{I_1 + I_2}{2} + \frac{I_1 - I_2}{2} \cos(2\theta) - I_{12} \sin(2\theta), \tag{15}$$

$$I_{xz} = \frac{I_1 - I_2}{2} \cos(2\theta) + I_{12} \sin(2\theta), \tag{16}$$

As given in the above equations, the moments of inertia in the $x'z'$ coordinate system can be computed after determining I_1, I_2, I_{12} and replacing the rotational angle (θ) with the twist angle (β) of the blade.

The bending stress at points P and Q can be computed by substituting the coordinates of points P and Q in Eq. (17):

$$(\sigma_{yy})_P = \frac{M_k(I_{zz}z'_P - I_{zx}x'_P)}{I_{zz}I_{xx} - I^2_{zx}}. \quad (17)$$

The computed bending stresses at points P and Q are plotted in Figure 9, where we can see that the bending stress reaches the maximum value at the blade root and around 50% blade span in the upper and lower skin.

As the flap-wise bending moment is maximum at the blade root, we can easily expect that the maximum bending stress happens at the blade root. In the current blade design, the blade is tapered and the blade thickness is reduced from the blade root to tip; accordingly, the second inertia of the moment of the blade decreases from root to tip. In Eq. (17), even though the flap-wise bending moment is not maximum at 50%L, if the second inertia of the moment is reduced too much, a high bending stress may happen at this location as well as at the blade root.

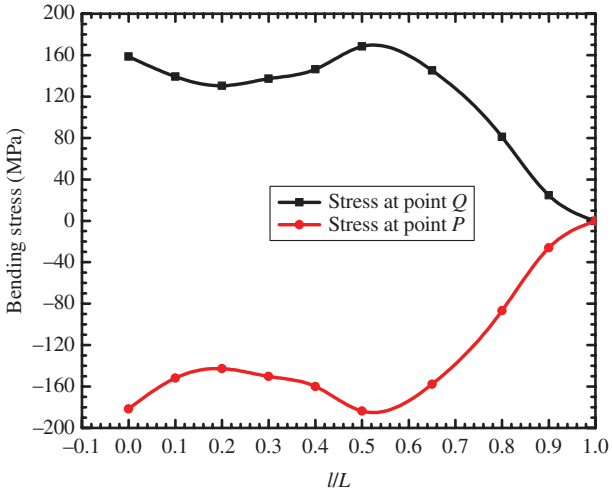

Figure 9: Bending stress distribution along the blade span.

5 Material selection

Figure 9 indicates that the maximum tensile stress may reach 170 MPa and that the maximum compressive stress can be >–190 MPa. Therefore, the materials used to fabricate the blade must possess tensile and compressive strengths that are larger than these stress levels. Table 2 summarizes the material properties of the selected materials. A glass/epoxy material was chosen instead of carbon fiber because carbon fiber is electrically conductive and is more susceptible to galvanic corrosion when coupled with fasteners, bolts, or nuts made of metals [21]. In particular, galvanic corrosion happens faster in an ocean environment, so it is better to use glass fiber materials for such cases. The glass/epoxy UD has a high tensile strength of 1.1 GPa and is mainly used to resist the bending stress along the blade span in the current design. However, the tensile strength in the lateral direction is very weak and is as low as almost 1/31 that in the fiber direction. The double-bias (DB) glass/epoxy is used to prevent delamination of the blade skin, and as it provides the same tensile strengths in both directions, it is used at the outer skin of the blade and is interleaved between the pack of UD layers. The DB layers are also useful to prevent skin buckling.

6 Results

As the bending stress distribution in Figure 9 identifies the two highest stress levels at the root and 50% blade span, it is essential to design a composite lay-up structure such that the structure can endure the stress levels that are present. The lay-up structures for the box beam structure of two spars and upper and lower skins are first suggested in Table 3, and the number of layers is properly reduced in the leading-edge and trailing-edge areas.

Finally, the lay-up structure and the loading conditions were applied to the finite element model of the blade structure in ANSYS Workbench. The finite element model was constructed using 36,000 four-node shell elements. The inner degrees of freedom at the roots of the two spars

Table 2: Characteristic of the fiber glass materials [27].

Material	Ply thickness (mm)	Density (kg/m³)	E_1 (GPa)	G_{12} (GPa)	σ_1^{ut} (MPa)	σ_1^{uc} (MPa)	ν_{12}
Double-bias	0.53	1830	9.0	3.2	150.0	–150.0	0.3
Unidirectional	0.53	1860	45.0	3.8	1100	–675.0	0.3

E_1, Elastic modulus in the fiber direction, G_{12}, in-plane shear modulus, σ_1^{ut}, ultimate tensile strength, σ_1^{uc}, ultimate compress strength, ν_{12}, Poisson's ratio.

Table 3: Preliminary lay-up structure of the blade.

Span location	Box structure			Leading edge and trailing edge		
	Number of layers		Thickness (mm)	Number of layers		Thickness (mm)
	DB	UD	DB+UD	DB	UD	DB+UD
0–20%	11	47	31.0	8	32	21.5
20–40%	10	37	25.4	7	22	15.4
40–60%	9	25	17.8	5	15	10.6
60–80%	7	15	11.7	4	10	7.4
80–100%	7	10	9.0	4	5	4.8

were constrained as the boundary condition. Figure 10 illustrates the forces and moment applied at each blade element, and Figure 11 shows the stress distribution of the stress in the span direction. The maximum stress can be seen to range from −42.176 to 33.27 MPa.

From the stress analysis based on the twisted box beam theory in the design stage, we expected that the maximum stress may happen near the blade root and 50%L location. Therefore, the composite layers were reinforced to avoid failure at these locations. Still, high σ_{11} was developed at these locations. The maximum stress happened at about 65%L, because the thickness of composite layers was additionally reduced after 50%L.

Table 4 summarizes the maximum failure indices of the five stress components, which were analyzed using ACP Pre and ACP Post composite material modules. The computed failure indices were found to be <0.4 for all stress components based on the maximum stress failure criteria [28].

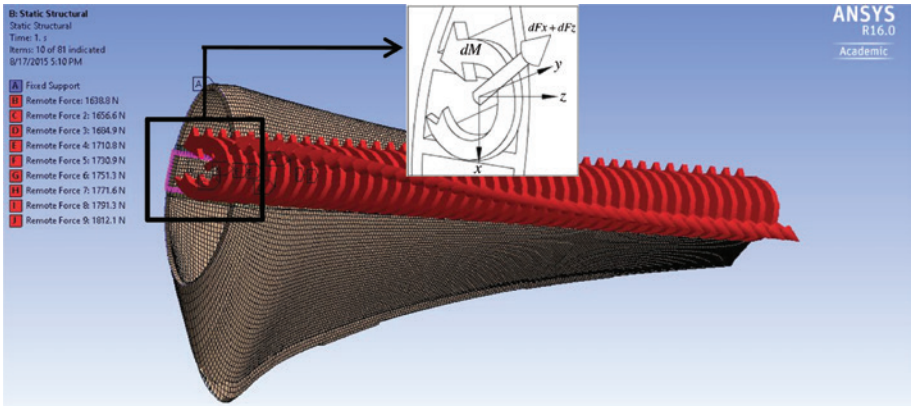

Figure 10: Loading condition at each blade section in the finite element model.

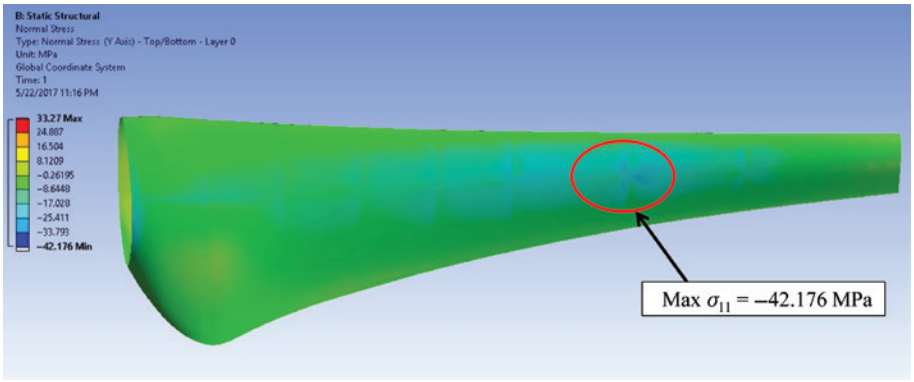

Figure 11: Distribution of the stress component in the span direction σ_{11}.

Table 4: Deformation and failure indices.

Maximum deformation	Parts	Failure indices (safety factor)				
		S_{11}	S_{12}	S_{22}	S_{31}	S_{23}
3.62%*R*	Skin	0.324	0.316	0.389	0.248	0.161
	Spar	0.277	0.319	0.29	0.265	0.088

The definition of the failure indices can be expressed as follows:

$$S_{11} = \frac{\sigma_{u11}}{\sigma^{t}_{11}} \text{ or } S_{11} = \frac{\sigma_{u11}}{\sigma^{c}_{11}}, \tag{18}$$

$$S_{22} = \frac{\sigma_{u22}}{\sigma^{t}_{22}} \text{ or } S_{22} = \frac{\sigma_{u22}}{\sigma^{c}_{22}}, \tag{19}$$

$$S_{12} = \frac{\tau_{u12}}{\tau_{12}}, \tag{20}$$

$$S_{31} = \frac{\tau_{u31}}{\tau_{31}}, \tag{21}$$

$$S_{23} = \frac{\tau_{u23}}{\tau_{23}}, \tag{22}$$

where σ_{uij}, σ^{t}_{ij}, σ^{c}_{ij}, τ_{uij}, and τ_{ij} are the ultimate stress in tension or compression, tensile stress, compressive stress, ultimate shear stress, and shear stress in the *ij* direction, respectively.

The failure indices obtained using finite element analysis show that the blade structure is expected to operate with safety factors as the inverses of the failure indices at >2.5. The lay-up structure can be optimized using an optimization process or refined via trial and error and experience.

7 Conclusion

In this work, we have proposed a design process for a composite blade structure intended for use in a HATT. The geometry of a 5-m-long blade was designed using the BEMT program with a NACA 63-424 hydrofoil. The blade was optimized to reach its maximum power coefficient at a *TSR* of 4.5. The maximum loading was chosen after the loading conditions for different inflow velocities were computed in the BEMT program. We then applied the beam theory to determine the initial thickness distribution of the blade, simplifying it as a twisted box beam. The failure index obtained through finite element analysis based on maximum stress criteria shows that the blade structure can be expected to operate with safety factors >2.5.

Acknowledgments: This research was supported by the project entitled "Development of active-controlled tidal stream generation technology" funded by the Ministry of Oceans and Fisheries, Korea (20110171).

References

[1] Charlier RH. *Renew. Sustain. Energy Rev.* 2003, 7, 515–529.
[2] Batten WMJ, Bahaja AS, Molland AF, Chaplin JR, Sustainable Energy Research Group. *Ocean Eng.* 2007, 34, 1013–1020.
[3] Bir GS, Lawson MJ, Li Y. *ASME 30th International Conference on Ocean, Offshore and Arctic Engineering*, 2011.
[4] Chen CC, Choi YD, Yoon HY. *IOP Conf. Ser. Mater. Sci. Eng.* 2013, 52, 052020.
[5] Grogan DM, Leen SB, Kennedy CR, Brádaigh CMÓ. *Renew. Energy* 2013, 57, 151–162.
[6] Honkonen K, Pierson S, Sale D, Tencer J. *Composite Rotor Design for a Hydrokinetic Turbine.* Tennessee Research and Creative Exchange, 2009.
[7] Sale D, Jonkman J, Musial W. *ASME 28th International Conference on Ocean, Offshore and Arctic Engineering*, 2009.
[8] Trudeau MG. *Structural and Hydrodynamic Design Optimization Enhancements with Application to Marine Hydrokinetic Turbine Blades.* BSc Thesis, 2011.
[9] Goundar JN, Ahmed MR. *Appl. Energy* 2013, 111, 161–174.
[10] Khan MJ, Bhuyan G, Iqbal MT, Quaicoe JE. *Appl. Energy* 2009, 86, 1823–1835.
[11] Laurens JM, Ait-Mohammed M, Tarfaoui M. *Renew. Energy* 2016, 89, 181–187.
[12] Schubel PJ, Crossley RJ. *Energies* 2012, 5, 3425–3449.
[13] Bryden IG, Grinsted T, Melville GT. *Appl. Ocean Res.* 2004, 26, 198–204.
[14] Amer C, Sahin M. *Int. J. Mech. Aeros. Indust. Mechatron. Manuf. Eng.* 2014, 8, 1264–1270.
[15] Chen K-N, Chen P-Y. *Int. J. Simul. Multidiscip. Design Optim.* 2012, 4, 159–165.
[16] Cox K, Echtermeyer A. *Energy Proc.* 2012, 24, 194–201.
[17] Locke J, Valencia U. *Design Studies for Twist-Coupled Wind Turbine Blades.* SAND2004-0522, 2004.
[18] Roth-Johnson P, Wirz RE, Lin E. *Renew. Energy* 2014, 71, 133–155.
[19] Kong C-D, Kim J-S. *KSAS Int. J.* 2000, 1, 92–102.
[20] Sale D, Aliseda A, Motley M. *Proceedings of the 1st Marine Energy Technology Symposium*, 2013.
[21] Anderson J, Hughes B, Johnson C, Stelzenmuller N, Sutanto L, Taylor B. *Capstone Project Report: Design and Manufacture of a Cross-flow Helical Tidal Turbine.* Project report, June 14, 2011.
[22] Phan LQ, Park HC, Ko JH, Le TQ. *Proceeding of the 10th International Conference on Intelligent Unmanned Systems*, 2014.
[23] Perfilev D. *Methodology for Wind Turbine Blade Optimization.* PhD Thesis, November 2013.
[24] Batten WMJ, Bahaj AS Molland AF, Chaplin JR. *Renew. Energy* 2008, 33, 1085–1096.

[25] Manwell JF, McGowan JG, Rogers AL. *Wind Energy Explained – Theory, Design and Application*, John Wiley & Sons Ltd.: Hoboken, NJ, USA, 2002.
[26] Timoshenko S, Young DH. *Element of Strength of Materials*, 5th ed., Van Nostrand: New York, 1968.
[27] ANSYS Workbench library v.16.0 academic version. *Composite Materials*.
[28] ANSYS Inc. *ANSYS Composite PrePost User's Guide*, v.15.0, November 2013.